Astronomy
&
Astrophysics

Performance study of ground-based infrared Bracewell interferometers

Application to the detection of exozodiacal dust disks with GENIE

O. Absil[1],[*], R. den Hartog[2], P. Gondoin[2], P. Fabry[2], R. Wilhelm[3], P. Gitton[3], and F. Puech[3]

[1] Institut d'Astrophysique et de Géophysique, Université de Liège, 17 Allée du Six Août, 4000 Sart-Tilman, Belgium
   e-mail: absil@astro.ulg.ac.be
[2] Science Payloads and Advanced Concepts Office, ESA/ESTEC, postbus 299, 2200 AG Noordwijk, The Netherlands
[3] European Southern Observatory, Karl-Schwarzschild-Str. 2, 85748 Garching bei München, Germany

ABSTRACT

Nulling interferometry, a powerful technique for high-resolution imaging of the close neighbourhood of bright astrophysical objets, is currently considered for future space missions such as Darwin or the Terrestrial Planet Finder Interferometer (TPF-I), both aiming at Earth-like planet detection and characterization. Ground-based nulling interferometers are being studied for both technology demonstration and scientific preparation of the Darwin/TPF-I missions through a systematic survey of circumstellar dust disks around nearby stars. In this paper, we investigate the influence of atmospheric turbulence on the performance of ground-based nulling instruments, and deduce the major design guidelines for such instruments. End-to-end numerical simulations allow us to estimate the performance of the main subsystems and thereby the actual sensitivity of the nuller to faint exozodiacal disks. Particular attention is also given to the important question of stellar leakage calibration. This study is illustrated in the context of GENIE, the Ground-based European Nulling Interferometer Experiment, to be installed at the VLTI and working in the L' band. We estimate that this instrument will detect exozodiacal clouds as faint as about 50 times the Solar zodiacal cloud, thereby placing strong constraints on the acceptable targets for Darwin/TPF-I.

Key words. instrumentation: high angular resolution – instrumentation: interferometers – techniques: interferometric – circumstellar matter – planetary systems

1. Introduction

The existence of extraterrestrial life in the Universe is a long-standing question of humankind. Future space missions such as Darwin (Fridlund 2000) or the Terrestrial Planet Finder Interferometer (Beichman et al. 1999; Lawson & Dooley 2005) are currently being studied respectively by ESA and NASA to search for evidence of life on Earth-like exoplanets by means of nulling interferometry (Bracewell 1978). These ambitious missions are particularly innovative from the technology point of view and demand several techniques to be first tested on ground. Both ESA and NASA have therefore initiated studies for ground-based infrared nulling interferometers (or "nullers"), to be installed respectively at the VLTI (Glindemann et al. 2004) or Keck Interferometer (Colavita et al. 2004). A cryogenic nulling beam-combiner is also under development for the LBT in the context of the NASA Origins Program (Herbst & Hinz 2004).

The principle of nulling interferometry, first proposed by Bracewell (1978) and generalized by several authors (Angel 1989; Léger et al. 1996; Angel & Woolf 1997; Karlsson & Mennesson 2000; Absil et al. 2003c), is to combine the light collected by two or more telescopes in a co-axial mode, adjusting their respective phases in order to produce a totally destructive interference on the optical axis. The interferometer is characterized by its transmission map $T_\lambda(\theta, \phi)$, displayed in Fig. 1 for a two-telescope interferometer, in one arm of which a phase shift of π radians has been introduced (*Bracewell interferometer*). Assuming that the field-of-view is limited by the diffraction pattern of a single telescope, its expression results from the fringe pattern produced by the interference between the beams, i.e., for a two-telescope interferometer:

$$T_\lambda(\theta, \phi) = \left(\frac{2J_1(\pi\theta D/\lambda)}{\pi\theta D/\lambda}\right)^2 \sin^2\left(\pi\frac{B\theta}{\lambda}\cos\phi\right), \qquad (1)$$

where θ and ϕ are respectively the radial and polar angular coordinates with respect to the optical axis, B the interferometer baseline, D the telescope diameter and λ the wavelength. In the

---
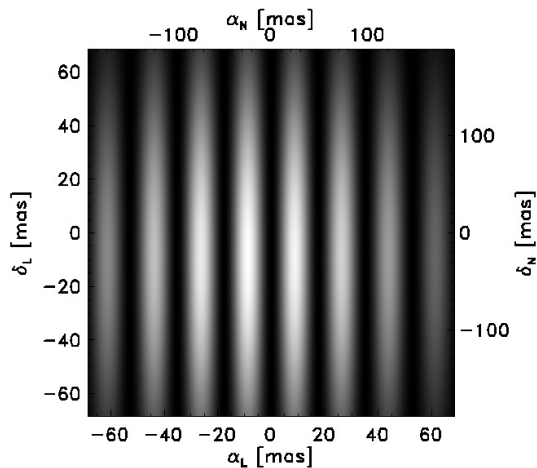
Fig. 1. Monochromatic transmission map for a 47 m Bracewell interferometer formed of two 8-m telescopes. The interferometric field-of-view, limited by the use of single-mode waveguides (see Sect. 3.3), is given by $\Omega = \lambda^2/S$ with S the telescope surface. Its diameter is respectively of 137 mas and 378 mas at the centers of the L' and N bands. The transmission map acts as a "photon sieve": it shows the parts of the field that are transmitted (white stripes) and those that are blocked (dark stripes, including the central dark fringe) by the interference process. The whole transmitted flux is integrated on a single pixel.

following study, we assume that recombination and detection are both done in the pupil plane, so that no image is formed: the flux is integrated on the field-of-view and detected on a single pixel. Performing the detection in an image plane would not significantly change the conclusions of this study.

Besides pure technology demonstration, ground-based nullers have an important scientific goal in the context of the Darwin/TPF-I missions, through the detection of faint circumstellar dust disks ("exozodiacal dust disks") around nearby main sequence stars. Such dust clouds may present a severe limitation to Earth-like planet detection with Darwin/TPF-I if they are more than 20 times as dense as the Solar zodiacal cloud (Absil 2001). A systematic survey of nearby main-sequence stars is thus mandatory to select convenient targets for these future space missions. Photometric surveys with infrared space telescopes such as IRAS, ISO and Spitzer have detected cold dust around nearby stars at a level of ∼100 times our Kuiper Belt, but did not allow the characterization of warm dust emission at a better level than about 500 times the Solar zodiacal cloud (Beichman et al. 2005). Attempts to spatially resolve faint exozodiacal clouds with single dish telescopes in the mid-infrared (Kuchner et al. 1998) and near infrared (Kuchner & Brown 2000) have not yielded better detection limits. Even the MIRI instrument onboard the future James Webb Space Telescope, equipped with coronagraphic devices at 10.6 μm and other longer wavelengths, does not have a good enough angular resolution (∼330 mas) to detect warm dust within the habitable zone of Darwin/TPF candidate targets.

Nulling interferometry, combining high dynamic range and high angular resolution, is particularly appropriate to carry out this systematic survey of the Darwin/TPF-I candidate targets. The Darwin target catalogue includes F, G, K and M-type main

sequence stars up to 25 pc (Stankov et al. 2005), with median distances to these four stellar types of respectively 20, 20, 19 and 15 pc. Ideally, the survey should detect exozodiacal clouds about 20 times as dense as the Solar zodiacal cloud ("20-zodi" clouds hereafter). Based on the model of Kelsall et al. (1998), such clouds are typically 10^4 times fainter than the star in the L' band (centered around 3.8 μm) or 10^3 times fainter in the N band (centered around 10.5 μm). The M band will not be considered in this study, because is too much affected by water vapor to be useful for nulling interferometry (Young et al. 1994).

Besides this survey aspect, ground-based nullers have various interesting scientific applications. Any target requiring both high dynamic range and high angular resolution will benefit from their capabilities, including the detection and characterization of debris disks around Vega-type stars, protoplanetary disks around Young Stellar Objects, high-contrast binaries, bounded brown dwarfs and hot extrasolar giant planets. Extragalactic studies may also benefit from ground-based nulling through the characterization of dust tori around nearby AGNs. Ground-based nullers are extremely powerful at angular diameter measurements as well: thanks to their very high stability, they could, for instance, detect pulsations in unresolved stars that still produce a non negligible stellar leakage in the nulled data.

In this paper, we estimate the performance of ground-based infrared nulling interferometers for the detection of exozodiacal dust around typical Darwin/TPF-I targets. The structure of the paper follows the path of the light, beginning with the astrophysical sources and ending up after detection with the data analysis procedures. In Sect. 2, we present the different contributors to the detected signals in ground-based nulling interferometry. Section 3 then focuses on a particularly important contributor (instrumental leakage), which strongly depends on the turbulent processes taking place in the Earth's atmosphere. We will show that this stochastic contributor needs to be compensated in real time at the hardware level in order to reach the required sensitivity. This has important consequences for the design of a ground-based nulling interferometer, as discussed in Sect. 4, where real-time control loops are addressed. After passing though the instrument and being recorded by the detector, the signal still needs to be carefully analyzed in order to extract the useful exozodiacal contribution from the raw data. Section 5 describes the associated post-processing techniques. In all these sections, we will take a Sun-like G2V star at 20 pc as a typical target for illustrative purposes. Finally, these concepts are applied in Sect. 6, where we derive the expected sensitivity of a specific instrument to the dust emission for different types of targets in the Darwin star catalogue.

2. Signals and noises in ground-based nulling interferometry

2.1. Exozodiacal dust disk

The Solar zodiacal cloud, a sparse disk of 10–100 μm diameter silicate grains, is the most luminous component of the solar system after the Sun. Its optical depth is only ∼10^{-7}, but its

integrated emission at 10 μm is about 300 times larger than the flux of an Earth-sized planet. Very little is known about dust disks around main sequence stars. We will thus assume that exozodiacal clouds have the same density distribution as the Solar zodiacal cloud, as described by Kelsall et al. (1998), but with a different scaling factor. In the following study, we will also assume exozodiacal disks to be smooth (no clump or wake in the disk) and to be seen face-on. With such assumptions, the azimuth of the baseline has no influence on the observations: only the baseline length matters, which is convenient for illustrative purposes. Nevertheless, we should note the influence of the disk shape on the transmitted signal.

– The *disk inclination* has a strong influence on the transmitted amount of exozodiacal light. If the disk is seen edge-on and oriented perpendicularly to the fringe pattern (i.e., major axis of the disk parallel to the baseline), it will produce almost the same transmitted signal as a face-on disk. However, if it is oriented in the same direction as the fringe pattern, a large part of the disk emission will be cancelled out by the central dark fringe. The azimuth of the baseline thus has a large influence on the detection of inclined disks, which is an advantage: if one lets the projected baseline evolve as an effect of the Earth diurnal rotation, the exozodiacal disk signal will be modulated as the baseline orientation changes, making the identification of the disk signal easier. The effect will be all the larger when the disk inclination is close to edge-on (Absil et al. 2003b).

– *Inhomogeneities* in the disk could lead to unexpected modulation as the baseline changes. In fact, the exozodiacal dust emission is expected to be smooth (less than 1% random variations) except for rings and wakes due to gravitational trapping by planets or bands due to recent asteroid or comet collisions (Dermott et al. 1998). The detection of such features would be a direct signature of the presence of planets or planetesimals in the disk. This would however require a good signal-to-noise ratio since these structures will be much fainter than the integrated disk emission.

2.2. Geometric stellar leakage

Even when the star is perfectly centered on the optical axis, a part of the stellar light still leaks through the transmission map due to the finite extent of the stellar disk, an effect known as geometric stellar leakage. We define the *nulling ratio N* as the ratio between the transmitted stellar flux and the total stellar flux collected by the two telescopes. Assuming that the stellar angular radius θ_* is small as compared to the fringe spacing λ/B, and computing the transmitted flux as a two-dimension integral of the transmission map on the stellar disk, one gets the following expression for the nulling ratio:

$$N = 1/\rho = \frac{\pi^2}{4}\left(\frac{B\theta_*}{\lambda}\right)^2, \tag{2}$$

assuming a uniform brightness across the stellar disk. The inverse of this quantity is called the *rejection rate ρ*, which is the fundamental figure of merit for a nulling interferometer. Typical values of the rejection rate for a Bracewell interferometer observing a Sun-like star at 20 pc are given in Table 1.

Table 1. Rejection rate for a Bracewell interferometer observing a Sun-like star at a distance of 20 pc in the L' and N bands, for typical interferometric baselines (14.4 m = LBT, 47 m = VLTI, 85 m = Keck). The star is assumed to be at zenith.

Baseline	14.4 m	47 m	85 m
L' band (3.8 μm)	22 197	2084	637
N band (10.5 μm)	169 573	15 897	4863

The rejection rate is quite sensitive to limb darkening, because it is precisely the outer parts of the stellar disk that mostly contribute to stellar leakage. Assuming a simple linear limb-darkening law $B_\lambda(\mu) = B_\lambda(1)[1 - u_\lambda(1 - \mu)]$ for the stellar surface brightness B_λ, with μ the cosine of the angle between the normal to the surface and the line of sight, the nulling ratio would be the following:

$$N_{\mathrm{LD}} = 1/\rho_{\mathrm{LD}} = \frac{\pi^2}{4}\left(\frac{B\theta_*}{\lambda}\right)^2\left(1 - \frac{7u_\lambda}{15}\right), \tag{3}$$

showing a linear dependance with respect to the limb-darkening parameter u_λ. For a typical K-band limb darkening $u_K = 0.26$ applicable to a Sun-like star (Claret et al. 1995), the rejection rate would increase by a substantial 14% assuming the same physical diameter in the uniform and limb-darkened cases. Other potential contributors to the actual amount of stellar leakage are the asymmetry of the stellar disk, through stellar oblateness and/or spots. However, these are only second order effects for late-type main-sequence stars, which are generally close to spherical symmetry and are expected to have only small and scarce spots. These effects will be neglected in the discussion.

Due to the limited rejection rate, geometric leakage will often exceed the flux from the exozodiacal disk at the destructive output of the nuller, especially in the L' band. Fortunately, geometric leakage is mostly deterministic, allowing the prediction of its contribution. This calibration procedure is discussed in Sect. 5.2.

2.3. Instrumental stellar leakage

The expression (3) of the rejection rate is valid only for a perfect Bracewell interferometer. In practice, the rejection rate is degraded by atmospheric turbulence and various instrumental effects causing imperfect co-phasing of the light beams, intensity mismatches and polarization errors (Ollivier 1999). This contribution, called *instrumental leakage*, adds to the geometric leakage at the destructive output of the interferometer. It is dominated by non-linear, second order error terms and does not depend on the stellar diameter to the first order (Lay 2004).

Instrumental leakage has two effects on the performance of the nuller: first, it introduces a *bias*, the mean contribution of instrumental leakage, and second, it introduces an *additional stochastic noise* through its fluctuations. While the second contribution can be reduced by increasing the observation time (see Sect. 4.4), the first one does not improve with time and limits the global performance of the nuller. Unlike geometric leakage, an analytical expression of instrumental leakage cannot
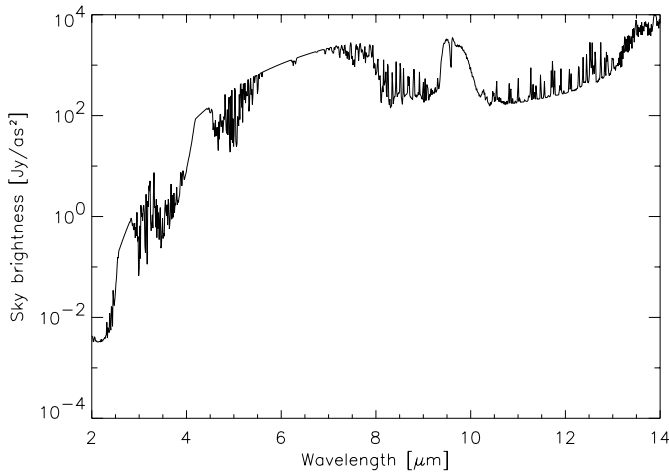
Fig. 2. Infrared sky brightness for typical Paranal atmospheric conditions.

be obtained: it depends on the particular shape and amplitude of the power spectral densities of various atmospheric effects and instrumental errors such as piston, dispersion, wavefront errors, polarization errors, etc. (Lay 2004). Its reduction can thus only be done through real-time control of these errors. In practice, instrumental leakage can be at least partially calibrated by observing "calibrator stars" with well-known diameters, a common method in stellar interferometry. This calibration, discussed in Sect. 5.3, will help remove the bias associated with the mean instrumental leakage and thereby relax the requirements on the performance of the real-time control loops.

2.4. The sky background

The thermal emission of the sky, which peaks in the mid-infrared, is obtained in good approximation by multiplying the Planck blackbody function by the wavelength-dependent sky emissivity. The infrared sky brightness is plotted in Fig. 2 for an atmosphere at a mean temperature of 284 K, which is typical for Cerro Paranal. The mean sky brightness in the relevant atmospheric wavebands is given in Table 4.

The fluctuation of the infrared background radiation produced by the atmosphere (or *sky noise*) has not been well modelled to date. Sky noise measurements have been carried out in the N band at Paranal with the VLTI mid-infrared instrument MIDI (Absil et al. 2004), while L'-band measurements have been carried out at Siding Springs, Australia (Allen & Barton 1981), showing that, at low frequencies, sky noise dominates over the shot noise associated with the mean background emission. Typical logarithmic slopes ranging from -1 to -2 have been recorded for the sky noise power spectral density (PSD).

2.5. The instrumental background

In order to conduct the light beams from the telescopes to the instrument, a large number of relay optics are used. All of them emit at infrared wavelengths. The wavelength-dependent emissivity of the optical train is theoretically equal to the

complementary of its transmission. In order to evaluate this contribution, we have to make some assumptions about the interferometric facility and nulling instrument. We will take the case of the VLTI, which has a transmission ranging between 30% and 40% in the near- and mid-infrared[1], and we will assume that the nulling instrument is at ambient temperature, except for the detection unit (spectrograph and detector). The instrumental background is given in Table 4, separated into "VLTI brightness" for the interferometric infrastructure and "GENIE brightness" for the nulling instrument, assuming an emissivity of 30% for the latter. A full cryogenic instrument would reduce the background emission, and thus improve the global sensitivity. However, even at ambient temperature, the full potential of the instrument can still be achieved by increasing the integration time, thereby reducing the contribution of the shot noise associated with the background emission. Fluctuations of the instrumental background are also expected to happen (e.g. due to beam wandering, mirror vibrations, gain fluctuations, etc.), but at a much lower level than sky noise. They will be neglected in the following discussion.

2.6. Detection criterion

In addition to the classical sources of noise such as shot noise, read-out noise and background noise, whose effect can be reduced by increasing the integration time, nulling interferometry is faced with two types of biases that must be removed to ensure a secure detection of the exozodiacal cloud. These biases are associated with the mean contribution of geometric and instrumental stellar leakage. In order to detect circumstellar features as faint as 10^{-3} (N band) to 10^{-4} (L' band) of the stellar flux with a signal-to-noise ratio of 5, *one should reduce the contributions of both geometric and instrumental stellar leakage down to 10^{-4} (N band) or 10^{-5} (L' band) of the initial stellar flux*, so that the total stellar leakage does not exceed about one fifth of the exozodiacal disk signal. Real-time control systems at hardware level and calibration techniques at software level will be used to reach this level of performance. The requirements on phase and intensity control will be particularly tight for short operating wavelengths. In the next section, the discussion of atmospheric turbulence is thus mainly illustrated in the L' band where its effects are the largest.

3. Influence of atmospheric turbulence

In order to estimate the performance of a nulling interferometer in the presence of atmospheric turbulence, we have developed a software simulator called *GENIEsim*[2] (Absil et al. 2003a). This semi-analytical simulator computes in real-time the transmission map of the interferometer, taking into account phase and intensity fluctuations associated with atmospheric turbulence. It inherently takes into account the bilinear error terms

---

[1] Due to the additional emission of dust particles located on the optics, the measured emissivity of the VLTI optical train is in fact closer to 100% than the expected 60–70%.

[2] GENIEsim, written in IDL, is open source and available on demand. Send request to R. den Hartog (`rdhartog@rssd.esa.int`).

discussed by Lay (2004) that are supposed to be the largest contributors to the instrumental nulling. In the following paragraphs, we describe the various sources of phase, intensity and polarization errors that have been implemented in the simulator and discuss their effect on instrumental nulling.

3.1. The piston effect

The 0th-order term of atmospheric turbulence, the spatially averaged phase perturbation on the pupil, is known as the piston effect. Optical path difference (OPD) fluctuations are mainly due to differential piston between the two apertures of the interferometer. Under the Taylor hypothesis of frozen turbulence, where a frozen phase screen is blown at the wind speed above the telescopes (Roddier 1981), the classical description of atmospheric turbulence proposed by Kolmogorov (1941) states that the temporal PSD of phase fluctuations follows a $-8/3$ power-law. In practice, three physical phenomena induce a departure from the theoretical $-8/3$ logarithmic slope (Conan et al. 1995): correlations between the pupils and the finite outer scale of turbulence $\mathcal{L}_0$ both reduce the fluctuations at low frequencies, while pupil averaging reduces them at high frequencies (Fig. 3). The latter effect has in fact never been observed, so that we keep the $-8/3$ slope at high frequencies as a conservative scenario. This scenario also features additional instrumental contributions:

- Bimorph piston effect: this is the OPD induced by resonances of the adaptive optics deformable mirror (Vérinaud & Cassaing 2001). This contribution has been evaluated for the MACAO adaptive optics at VLTI, and turns out to be dominant above 100 Hz despite the use of a "piston-free" algorithm for the control of the deformable mirror.
- Coupled piston: this is the additional OPD created by high-order wavefront errors when injecting the beams into single-mode waveguides (Ruilier & Cassaing 2001).

The standard deviation of the OPD fluctuations, neglecting the effect of the outer scale, is given by (Roddier 1981):

$$\sigma_{\text{OPD}} = 2.62 \frac{\lambda}{2\pi} \left(\frac{B}{r_0} \right)^{5/6}. \tag{4}$$

Since the Fried parameter r_0 is proportional to $\lambda^{6/5}$, σ_{OPD} does not depend on wavelength. For a typical baseline of 47 m and $1''$ seeing, the theoretical variance of piston is about 35 μm, i.e., about 9 fringes in the L' band. This variance, which is also the area under the dotted curve in Fig. 3, sets the level of the PSD.

The effect of phase errors on a Bracewell nulling interferometer is to shift the position of the fringes in the transmission map: the dark fringe is not centered any more on the optical axis. For a small phase error $\epsilon_\phi(\lambda)$ between the two beams, the shifting of the dark fringe produces a non-null on-axis transmission $T_\lambda(0,0) = \epsilon_\phi(\lambda)^2/4$ (Ollivier 1999). In order to keep the instrumental rejection rate above the required 10^5 in the L' band, the phase error should be smaller than 0.006 radian (i.e., 4 nm in the L' band), while atmospheric piston induces OPD errors of about 35 μm. A deep and stable null can thus
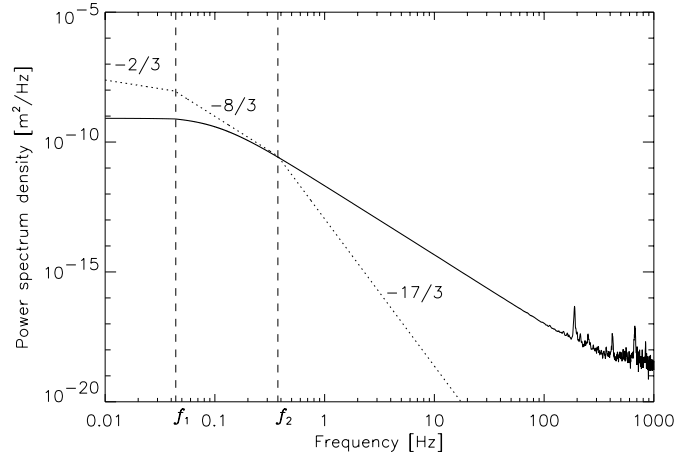

Fig. 3. Differential piston power spectrum, under the following conditions: $B = 47$ m, $D = 8$ m, $v = 11$ m/s and $r_0 = 10$ cm at 500 nm (equivalent to $1''$ seeing). The dotted line represents the theoretical Kolmogorov piston PSD, showing the effects of pupil correlations (below $f_1 \simeq 0.2v/B$) and pupil averaging (above $f_2 \simeq 0.3v/D$), but without the effect of the outer scale nor the instrumental contributions. The solid line is the representation of the piston PSD that we actually use in our simulations as a conservative scenario. It includes the effect of pupil correlations and of the outer scale of turbulence (flattening of the PSD for frequencies below $v/\mathcal{L}_0$), as well as the contributions of bimorph and coupled piston (high-frequency fluctuations), but excludes pupil averaging. A best-case scenario would correspond to the combination of the dotted line for $f > f_2$ and the solid line for $f < f_2$.

only be achieved by stabilizing the dark fringe on the optical axis, by means of a fringe tracker (Sect. 4.1).

3.2. Longitudinal dispersion

In addition to the achromatic piston effect produced by the fluctuations of the air refractive index, another source of phase errors comes from the fluctuation of the water vapor column densities above the two telescopes. A useful concept to describe the column density fluctuations of water vapor is "Water-vapor Displacing Air" (WDA), introduced by Meisner & Le Poole (2003). The fluctuation of the WDA column density induces a chromatic OPD difference between the beams, because its refraction index n_{WDA} strongly depends on wavelength in the infrared as illustrated in Fig. 4. This effect, referred to as *longitudinal dispersion*, has the same kind of influence on the transmission map as the piston effect, except that the offset of the dark fringe is now wavelength-dependent. This has two deleterious consequences on the performance of a nulling instrument:

- *inter-band dispersion* is the phase error measured at the center of the science waveband assuming that piston is perfectly corrected at another wavelength by means of a fringe tracker (this correction is generally done in the H and/or K band, e.g. at the Keck and VLT interferometers);
- *intra-band dispersion* refers to the differential phase error within the science waveband: if one manages to co-phase the beams at the central wavelength of the science waveband, their phases will not be perfectly matched at the edges of the band.
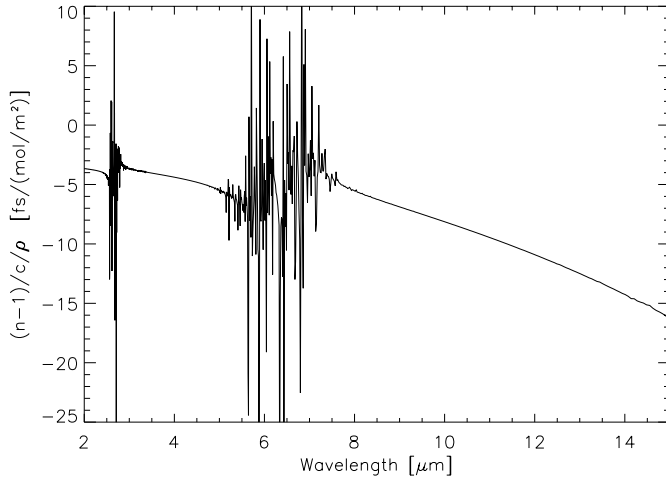
Fig. 4. Reduced refraction index of WDA ($\hat{n}_{\text{WDA}} = \frac{n_{\text{WDA}}-1}{c\rho}$, with c the speed of light and ρ the molar density) expressed in femtosecond per mole/m², plotted at infrared wavelengths.

Fig. 5. PSD for tip-tilt before (dotted line) and after (solid line) close-loop control with MACAO. The peaks at high frequencies are induced by mechanical resonances in the deformable mirror.

Since longitudinal dispersion is produced by the same turbulent atmosphere as piston, it is expected to follow the same theoretical PSD. This has been confirmed experimentally by Lay (1997). An rms value of 1.5 mole/m² for the column density fluctuation of water vapor has been measured by Meisner & Le Poole (2003) at Paranal on an integration time of 100 s (this value corresponds to 27 μm rms of differential precipitable water vapor). This translates into typical inter-band and intra-band OPD errors of 550 nm and 150 nm rms respectively in the L' band assuming that fringe tracking is performed in the H band. A control system must thus be devised to stabilize the dark fringe on the optical axis in order to meet the requirements on the instrumental rejection rate.

3.3. Wavefront errors

Propagation through the turbulent Earth atmosphere degrades the shape of the wavefronts, producing imperfect interference between the beams at recombination, and thus creates a halo of incoherent stellar light at the detector. Modal filtering by means of single-mode fibers, as proposed by Mennesson et al. (2002), eliminates wavefront corrugations by projection on the fundamental mode of the fiber, thereby ensuring perfect matching of the wavefronts over a broad bandpass. After injection into a single-mode fiber, the shape of the initial wavefront only affects the amount of energy coupled into the guide. *The modal filter thus converts phase defects into intensity errors*, which are less severe for a nulling interferometer (Ollivier 1999). It also induces a small coupled piston due to the non-null mean of $z > 1$ Zernike polynomials projected onto the Gaussian fundamental mode of the fiber (Ruilier & Cassaing 2001). The use of single-mode fibers to filter the beams at the focus of the telescopes strongly relaxes the constraints on pointing accuracy and low order aberrations, and thus improve the capability to achieve deep rejection ratios. We will assume that modal filtering, or at least spatial filtering using pinholes for the N band, is used in our nulling interferometer.
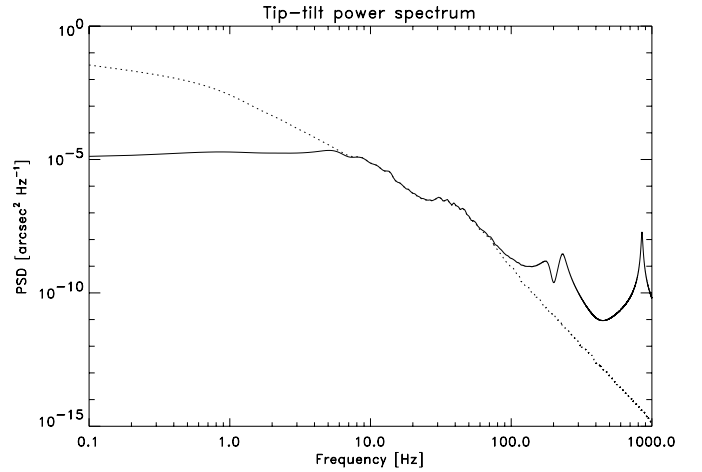
In the following study, we will also assume that the telescopes are equipped with adaptive optics, with performance similar to that of the MACAO systems on ESO's Very Large Telescopes (Arsenault et al. 2003). The power spectral densities of individual Zernike modes are taken from Conan et al. (1995), with typical high-frequency slopes of $-17/3$ and various slopes at low frequencies. These PSDs are corrected by the adaptive optics servo system for frequencies below about 10 Hz, thereby making their low-frequency content negligible. The case of tip-tilt is illustrated in Fig. 5, including the contribution of high order Zernike modes (ten Brummelaar 1995). The values for the rms tip-tilt and Strehl are given in Table 2.

The coupling efficiency η into a single-mode fiber is computed by taking into account two contributions: the tip-tilt error which induces an offset of the stellar Airy pattern with respect to the fiber core (assuming the on-sky tip-tilt to be perfectly translated into an on-fiber jitter), and the Strehl ratio which represents the coherent part of the beam and can be taken as a multiplicative factor in the computation of coupling efficiency (Ruilier & Cassaing 2001). The mean and rms coupling efficiencies after correction by adaptive optics are given in Table 2.

The effect of coupling efficiency fluctuations, which produce unequal intensities in the two arms of the interferometer, is to induce a non-null transmission on the optical axis. Letting ϵ_I be the relative intensity error between the two beams, the expression of the central transmission is $T_\lambda(0,0) = \epsilon_I^2/16$ (Ollivier 1999). In order to keep the instrumental rejection rate above the required 10^5, relative intensity errors should be smaller than 1%, while the AO-corrected atmospheric turbulence induces intensity fluctuations as high as 8% in the L' band. A servo loop for intensity matching is therefore necessary to obtain a deep and stable null in the L' band. Such a device is not needed in the N band, where relative fluctuations of 1% are expected.

Table 2. rms tip-tilt, mean and rms Strehl ratio for an 8-m telescope after correction by MACAO, as simulated by GENIEsim under typical atmospheric conditions at Cerro Paranal (1″ seeing, 11 m/s wind speed). The mean and rms coupling efficiencies into a single-mode fiber are deduced (taking into account the effect of central obscuration).

	Average	Std deviation
Tip-tilt [mas]	0	14
Strehl L' band	0.80	0.050
Strehl N band	0.97	0.008
Coupling L' band	0.58	0.044
Coupling N band	0.77	0.008

3.4. Scintillation

Scintillation is the effect of rapid intensity fluctuations of a point-like source as a result of the interference of light rays diffracted by turbulent cells. The condition for scintillation to take place is that the Fresnel scale $r_F = (\lambda h \sec z)^{1/2}$ is larger than the Fried scale r_0, with h the height of the turbulent layer and z the zenith distance (Quirrenbach 1999). Even for high turbulent layers (20 km) and large zenith distances ($z = 45°$), we obtain $r_F \simeq 0.3$ m while $r_0 \simeq 1.1$ m in the L' band for 1″ seeing, showing that the Fried parameter is always larger than the Fresnel scale. Numerical estimates obtained with GENIEsim confirm this statement: scintillation does not induce intensity fluctuations larger than 0.2% in the L' band. Since $r_0 \propto \lambda^{6/5}$ while $r_F \propto \lambda^{1/2}$, scintillation is also negligible for longer wavelengths, including the N band.

3.5. Polarization errors

The polarization errors encountered by a nulling interferometer are of three main types: differential phase shift, differential attenuation and differential rotation can occur between the two beams for each linear polarization component. These effects can be translated into phase and intensity errors, but unlike phase and intensity errors due to turbulence, they are only due to the instrument itself. Polarization errors are thus expected to be mainly static or slowly drifting, even if instrumental vibrations might induce some fluctuations. A highly symmetric design of the whole interferometer is required to reduce polarization issues as much as possible (Serabyn & Colavita 2001). In the following study, we will assume that the nulling instrument is designed so as to keep this contribution negligible in the instrumental leakage budget. This may not be the case in practice, because existing interferometers are not necessarily designed to meet the tight tolerances on polarization associated with nulling interferometry. This might force the nuller to operate in polarized light, by inserting polarizers at the beginning of the optical train[3] and just before recombination. The instrumental throughput would then be reduced by 50%, thereby increasing the required integration times.

---

[3] In practice, a polarizer cannot be put in front of the primary or secondary mirror of a telescope, so that the first few mirrors of the optical train could still contribute to polarization errors.
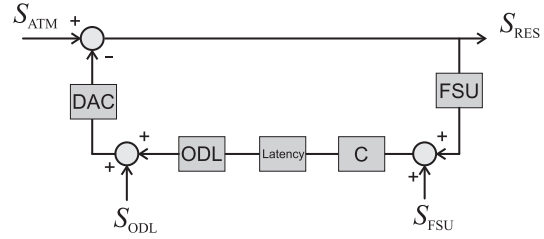
Fig. 6. Simplified block-diagram of a fringe tracking system: the OPD error between two beams, characterized by its PSD S_{ATM}, is sampled by a fringe sensing unit (FSU) feeding an OPD controller (C), which computes the correction to be applied by the optical delay line (ODL). The latency represents the effect of the finite CPU and electronics time required between fringe sensing and correction, while the digital-to-analogue converter (DAC) represents the conversion from a digital command to an analogue OPD correction by the delay line. The OPD power spectrum after closed-loop control is denoted S_{RES}, while the noise introduced by the FSU and the ODL are respectively S_{FSU} and S_{ODL}.

4. Real-time control and instrumental design

We have seen that atmospheric turbulence causes additional stellar photons to leak through the null (*instrumental leakage*), and that this bias cannot be calibrated analytically as for geometric leakage. Moreover, the stochastic fluctuation of instrumental leakage is the source of an important noise contribution, called *systematic noise* (Lay 2004) or *variability noise* (Chazelas et al. 2005). This section describes the three major control systems that are needed to reduce instrumental leakage and variability noise down to an acceptable level by correcting the effects of atmospheric turbulence in real time. As discussed in Sect. 3 and summarized in Table 3, an instrumental rejection rate of 10^5 requires the residual phase and intensity errors to be smaller than 4 nm and 1% rms respectively. If this level of performance cannot be met, the use of calibrator stars will be further investigated to estimate and remove the contribution of instrumental leakage.

4.1. Fringe tracking

The purpose of a fringe tracker is to actively compensate for random phase fluctuations between the beams of the interferometer at a given wavelength. A fringe sensing unit (FSU) measures the phase difference at a given sampling frequency and transmits this information to a controller which computes the compensation to be applied to one of the beams by an optical delay line (ODL), as illustrated in Fig. 6. Both the FSU and the ODL introduce noise in the fringe tracking control loop, while the controller is (almost) noiseless. In order to be efficient, fringe tracking requires a high signal-to-noise ratio to be achieved on phase measurements on very short time scales (typically between 0.1 and 1 ms). It is therefore usually performed in the near-infrared ($\lambda < 2.4\ \mu$m) where stellar photons are numerous and the sky background rather low.

Large interferometric facilities such as the VLTI or Keck Interferometer are (or will soon be) equipped with fringe trackers. For instance, FINITO and PRIMA at VLTI will deliver
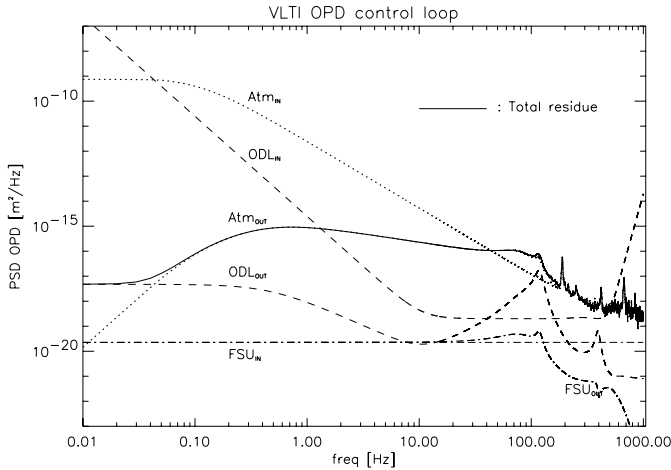
Fig. 7. Simulation of the VLTI OPD control loop. The plot gives the PSDs at the input (before actuation: subscript "IN") and output (after actuation: subscript "OUT") of the loop for the three noise sources in the VLTI fringe tracking loop, i.e., atmospheric fluctuations (Atm, dotted curves), fringe sensing (FSU, dashed-dotted curves) and optical delay line (ODL, dashed curves). The total closed-loop OPD jitter (area under the solid line) is 133 nm rms for a repetition frequency of 4 kHz.

a residual OPD of about 150 nm rms on bright stars, respectively in the H and K bands (Wilhelm & Gitton 2003). However, this is not sufficient to meet our goal on OPD stability, implying that a second stage of OPD control must be implemented inside the nulling instrument. In fact, the main limitation to the accuracy of the VLTI fringe tracker comes from the ODL, which does not efficiently correct for OPD fluctuations at frequencies higher than 50 Hz (see Fig. 7). The main requirement for the additional fringe tracker is thus to be equipped with a low-noise ODL optimized for high repetition frequencies (up to 20 kHz).

We have simulated the performance of a fringe tracker optimized to achieve small residual OPD on bright stars. The fringe tracker features a fringe sensor working both in the H and K band and uses a short-stroke fast piezo or voice-coil delay line to compensate the remaining OPD fluctuations. The control loop parameters are computed through a simultaneous optimization of the repetition frequency and of the controller parameters (a simple PID[4]). The repetition frequency has been artificially limited to 20 kHz to comply with state-of-the-art back-end electronics. The delay line is assumed to have a perfect response up to this frequency (short-stroke piezo translators can achieve this kind of performance). The OPD control performance, summarized in Table 3, is computed in two cases:

- the *worst case* corresponds to a $-8/3$ slope for the turbulence PSD at high frequencies (see Fig. 3) and includes the bimorph piston effect;
- the *best case* takes into account the effect of pupil averaging on the PSD ($-17/3$ slope at high frequencies) and does not include the bimorph piston effect.

---

[4] PID stands for "Proportional, Integral and Differential" and is a basic controller for closed-loop control.

Table 3. Performance of an L' band nuller at VLTI as simulated with GENIEsim on a 100 s observation block, taking into account all turbulence-induced errors. The performance of the control loops are summarized together with their repetition frequencies in pessimistic and optimistic cases (see text). The target performance discussed in Sect. 3 appears in the last column. The total null is the mean nulling ratio including both the geometric and instrumental leakage contributions, and is computed as the ratio between the total input and output stellar fluxes (from both telescopes). The last line gives the standard deviation of the instrumental nulling ratio for this 100 s observation block.

	Worst case	Best case	Goal
Piston	17 nm @ 20 kHz	6.2 nm @ 13 kHz	<4 nm
Inter-band	17 nm @ 200 Hz	4.4 nm @ 300 Hz	<4 nm
Intra-band	4.1 nm @ 200 Hz	1.0 nm @ 300 Hz	<4 nm
Intensity	4% @ 1 kHz	4% @ 1 kHz	<1%
Total null	9.7×10^{-4}	6.2×10^{-4}	4.8×10^{-4}
Instr. null	5.0×10^{-4}	1.5×10^{-4}	10^{-5}
rms null	5.8×10^{-4}	1.6×10^{-4}	10^{-5}

The predicted performance ranges between 6 nm and 17 nm rms. These figures could be improved by using a priori knowledge on the behaviour of atmospheric turbulence in the control process, e.g. through Kalman filtering. First estimates have shown an improvement of about 2 nm on the residual OPD with respect to the above numbers (C. Petit, personal communication). This performance, summarized in Table 3, is marginally compliant with the required 4 nm rms.

4.2. Compensation of longitudinal dispersion

There are two different sources of dispersion to be corrected: the slowly varying differential phase due to unequal paths through wet air in the delay lines, and an additional rapid phase fluctuation due to column density fluctuations of dispersive components in the atmosphere. The first one is deterministic and easy to correct provided that the atmospheric conditions are monitored in the delay lines, while the second one is the real problem and is mainly associated with water vapour, as well as other molecular species such as ozone, carbon dioxide, etc., which are the main contributors below 2.5 μm (Mathar 2004).

In order to correct for both inter-band and intra-band dispersion (Sect. 3.2), one should measure the differential column density of water vapour experienced by the two beams in their paths through the atmosphere. This quantity can be inferred by measuring the phase difference between the beams at two different wavelengths, using the knowledge of the refractive index of wet air across the infrared. In practice, a blind phase correction in the science band, relying for instance on H- and K-band measurements, is dangerous because it is not sensitive to possible biases, e.g. related to the imperfect knowledge of the refraction index or to the presence of other dispersive gases (Meisner & Le Poole 2003). Phase measurements in the science band are thus necessary to ensure a good co-phasing,

using a part of the scientifically useful signal. These measurements will be carried out at a slower rate, on one hand because of the lower signal-to-noise ratio on phase measurements at longer wavelengths and on the other hand because the possible biases related to the extrapolation of the phase delay from the H/K bands towards longer wavelengths are mainly affected by global atmospheric parameters (temperature, partial pressures of gases, etc.) which are not expected to evolve quickly during the night. Another possibility would be to perform both fringe tracking and dispersion control by using science-band photons exclusively, in order to reduce the technical complexity of the instrument. This would however lead to slightly reduced performance, due to the worse signal-to-noise ratios on phase measurement at longer wavelengths, and would even become impractical in the N band.

Interferometric facilities are currently not equipped with an active dispersion compensation device, which should thus be integrated in the nuller itself. The required correction is two-fold: the inter-band phase error should be corrected with a dedicated short-stroke delay line (less than 1 μm rms to be compensated), while intra-band dispersion could be corrected by introducing a variable amount of dispersive material in the beams to correct for the slope of the phase inside the science waveband (Koresko et al. 2003). The performance of such a correction system is summarized in Table 3 in the L' band, once again in two cases:

- the *worst case* is obtained by assuming that phase measurements in the L' band are needed at each step of the control process, and assuming a $-8/3$ slope for the high-frequency asymptote of the atmospheric turbulence PSD;
- the *best case* is computed assuming that H/K band phase measurements are sufficient for dispersion control and that the input PSD has a $-17/3$ slope at high frequencies.

The closed-loop performance ranges between 4.4 nm and 17 nm rms for inter-band dispersion, between 1.0 nm and 4.1 nm rms for intra-band dispersion. It is marginally compliant with the requirement (4 nm rms).

4.3. Intensity matching

The third real-time control loop to be implemented in the nulling instrument is a device to correct for unequal intensities between the two beams. In fact, intensity fluctuations are not a problem per se: it is only the differential fluctuations between the beams that matter. The most straightforward way to compensate for this effect is to measure the intensities of the two beams, determine which one is the brightest and reduce its intensity down to the level of the other one by means of an actuator. This correction must take into account the effect of coupling into single-mode fibers, so that the intensity sensors must also be placed after the modal filters. Furthermore, it must be carried out in the science waveband, because coupling efficiency is wavelength-dependent. We will thus "waste" an additional part of the useful signal for intensity control. A possible actuator could consist in a piezo-driven adjustable iris, which would reduce the beam size in a pupil plane while keeping it
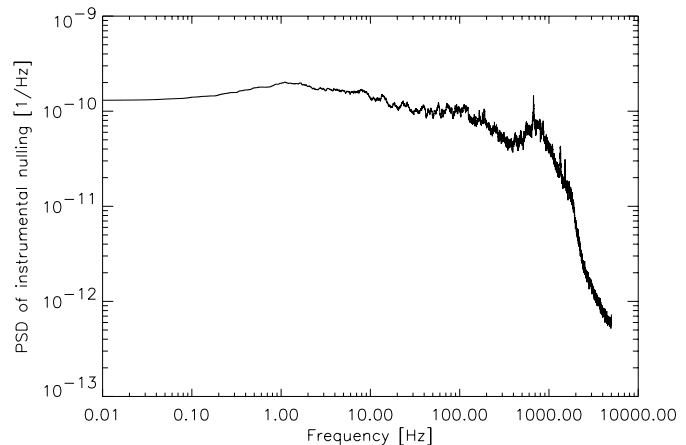
Fig. 8. Power spectrum of instrumental nulling due to phase and intensity errors after closed-loop control, obtained for a 100 s simulation with GENIEsim in the L' band. The semi-analytical simulation takes into account the bilinear error terms discussed by Lay (2004), but not the possible $1/f$-type noises discussed by Chazelas et al. (2005). The power spectrum has been smoothed with a standard IDL routine to show its mean behaviour: almost flat at low frequencies, while the logarithmic slope at high frequencies is about -2.

(almost) circular to preserve injection properties as much as possible.

The closed-loop control performance is summarized in Table 3 for the L' band, with a typical residual intensity mismatch of 4% when the loop is running at 1 kHz. This performance does not meet the required 1% mismatch, which makes additional calibrations mandatory (see Sect. 5.3). Note that this control loop does not remove the fluctuations of the mean coupling efficiency (common to both beams), which has a typical standard deviation of 8%.

4.4. Instrumental nulling performance

Table 3 shows the nulling performance associated with the residual phase and intensity errors after closed-loop control for a G2V star at 20 pc. The rms instrumental nulling ratio corresponds to the concept of variability noise (Chazelas et al. 2005). Its power spectrum is illustrated in Fig. 8, showing an almost flat spectrum for frequencies below 1 kHz and a rapid decrease of the power content above 1 kHz. Variability noise thus behaves as a white noise at typical read-out frequencies ($\sim$10 Hz), so that its cumulated contribution increases as the square root of integration time just as for shot noise. We do not take into account here the possible $1/f$-type noises (Chazelas et al. 2005), which might alter the slope of the PSD at low frequencies and thus change the behaviour of long-term variability noise by introducing more power at low frequencies. This assumption is supported by the use of real-time control loops, which will help remove possible drifts in the instrumental response.

5. Post-processing of nulling data

Because the expected performance of state-of-the-art real-time control loops is not sufficient to reduce instrumental leakage down to the required level (10^{-5} in the L' band), and because other sources such as geometric leakage and background also

contribute to the detected signal after destructive beam combination, the exozodiacal disk signal can only be extracted from the raw data after a final and critical phase of correction: post-processing.

5.1. Background subtraction

The first step in the data analysis procedure is to remove the contribution of the background. In order to extract the useful data from the incoherent background in the nulled data, modulation techniques are required. The classical "chopping-nodding" technique consists in tilting the secondary mirror by a small quantity (a few arcseconds) in order to measure the background in an empty sky region close to the source and subtract it from the on-source measurement. The chopping sequence is repeated at a few Hertz. Nodding consists in repeating the whole chopping sequence off-source, by slightly tilting the telescope, in order to remove the possible gradient in the background emission.

Because of the large temporal fluctuations of the background emission, chopping at a few Hz is not sufficient to reduce sky noise below the level of the scientifically useful signal after background subtraction. Other techniques are therefore considered in order to measure the background emission simultaneously to the observations, e.g. by inserting additional fibers in the transmitted field-of-view of the interferometer. At VLTI for instance, the use of variable curvature mirrors in the delay lines provides a clean field-of-view $2''$ in diameter, which allows us to reduce the contribution of stellar light in the background fibers down to about 10^{-4} of the background contribution. Another solution for background subtraction is to use phase modulation techniques, which require the telescope pupils to be divided into two parts in order to modulate between two different nulled outputs (Serabyn et al. 2004). This is the only practical solution for an N-band nuller, for which the contrast between background and exozodiacal fluxes is huge (almost 10^7, see Table 4).

5.2. Geometric leakage calibration

An important step in the post-processing of nulling interferometry data is the calibration of geometric leakage. We have discussed in Sect. 2.6 that the residual contribution of geometric leakage after calibration should not exceed 10^{-5} of the initial stellar flux in the L' band, while typical rejection rates of 2000 are expected (Table 1). The calibration of geometric leakage, based on the analytical expression (3) of the rejection rate, should therefore reach a precision of about 2% in order to retrieve the useful exozodiacal disk signal with a good signal-to-noise ratio. Closer stars, for which the rejection rate is smaller, require even better calibration accuracies. *A typical precision of 1% for geometric leakage calibration is thus required in the L' band*, while such a calibration is marginally needed in the N band since the achievable rejection rate ($\sim$16 000) already matches the requirement on starlight rejection (10^{-4}).

Assuming that the baseline B and the effective wavelength λ are known with a good accuracy, a good knowledge of the stellar angular radius θ_* and limb-darkening coefficient u_λ is sufficient in order to compute the geometric leakage. The global optical transmission of the interferometer must also be known in order to convert this value into a number of photo-electrons measured at the detector. While the interferometric transmission can be straightforwardly measured with a high precision at the constructive output of the nuller where most of the stellar photons end up, the imperfect knowledge of stellar diameters has a large (and generally dominant) contribution to the calibration error budget. Differentiating Eq. (3), we obtain a required precision $\Delta\theta_*/\theta_* = 0.5\Delta N/N = 0.5\%$ on the stellar diameter knowledge.

The most precise way to determine stellar angular radii is currently based on stellar interferometry. Stellar diameter measurements with an accuracy as good as 0.2% have been demonstrated on resolved stars such as α Cen A and B (Kervella et al. 2003). However, the Darwin/TPF-I targets, with typical angular diameters of 1 mas and below, are only marginally resolved even with the longest baselines currently available: the AMBER instrument at VLTI provides at best an angular resolution of 1.6 mas in J band. A precision of a few 0.1% on diameter measurements with AMBER could thus only be achieved for the closest stars in the Darwin catalogue ($<$10 pc). An additional difficulty comes from the extrapolation of the limb-darkening law from the J band to the L' band, since limb-darkening coefficients are currently modelled only up to the K band (Claret 2000). Lunar occultation measurements could also be used to determine the diameters of the brightest targets of the Darwin catalogue ($K \sim 3$) with a limiting resolution of $\sim$1 mas, but with the restriction that only about 10% of the sky falls on the Moon's path (Fors et al. 2004).

For stars more distant than about 10 pc, for which interferometric diameter measurements will probably not reach a 0.5% precision, indirect measurements based on surface brightness relations might be used. Empirical laws make it possible to predict the limb-darkened angular diameters of dwarfs and subgiants using their dereddened Johnson magnitudes, or their effective temperature (Kervella et al. 2004). Intrinsic dispersions as small as 0.3% are obtained for the relations based on $B - L$ magnitudes. However, the apparent magnitudes of the Darwin/TPF-I targets need to be accurately known (to better than 0.02 mag): this is usually not the case at infrared colours and might mandate a dedicated photometry programme.

All in all, it is expected that diameter measurements with a precision of 0.5% will be obtained on most of the Darwin/TPF-I targets. A 1% precision is still considered as a worst case scenario in the performance budget.

5.3. Instrumental leakage calibration

After calibration of geometric leakage, there is one remaining step of calibration to be carried out: the evaluation and subtraction of the mean instrumental leakage from the nulled data. Calibration of the instrumental response is a routine procedure in stellar interferometry, and is achieved by observing a

well-know *calibrator star*, usually chosen as a late-type un-resolved giant star (Mérand et al. 2005). These measurements are carried out just before and after the observation of the target star, and as close as possible to it in the sky, so that the atmospheric properties do not change significantly.

This method can be extended to measure instrumental leakage in nulling interferometry. In this case, calibrator stars must be carefully chosen: even if instrumental leakage does not depend on the angular diameter of the star to the first order, the control loop performance strongly depends on the stellar flux and spectrum, so that the calibrator star should in fact have the same flux and spectrum as the target star in order to get the same instrumental leakage in both cases. Having the same flux and spectrum means that the angular diameters should also be the same, and consequently that the calibrator star will produce the same amount of geometric leakage as the target star. A precise knowledge of the calibrator's angular diameter is thus needed in order to remove the contribution of geometric leakage and obtain a good estimation of instrumental leakage.

The final estimation $Z(\lambda)$ of the exozodiacal signal after both geometric and instrumental leakage calibrations can be expressed as follows:

$$Z(\lambda) = S_t(\lambda) - \frac{\pi^2 B^2 \theta_t^2}{4\lambda^2} F_t(\lambda) - \frac{F_t(\lambda)}{F_c(\lambda)} \left(S_c(\lambda) - \frac{\pi^2 B^2 \theta_c^2}{4\lambda^2} F_c(\lambda) \right), \quad (5)$$

with $S_t(\lambda)$ and $S_c(\lambda)$ the background-subtracted nulled fluxes for the target and calibrator stars, θ_t and θ_c their angular radii, $F_t(\lambda)$ and $F_c(\lambda)$ their fluxes, measured at the constructive output of the interferometer. The first subtracted term represents the contribution of geometric leakage while the second one (between brackets) is the estimation of instrumental leakage obtained with the calibrator star.

6. Detection of exozodiacal dust disks with GENIE

In the following paragraphs, we evaluate the sensitivity of GENIE, the Ground-based European Nulling Interferometer Experiment (Gondoin et al. 2004), to exozodiacal dust for typical Darwin/TPF-I targets.

6.1. Background-limited signal-to-noise ratio

Before computing the actual detection performance of the nuller, let us assess the required integration times in a non-turbulent environment, where the only source of noise is the shot noise from all sources inside the field-of-view. The photon budget of Table 4 includes the geometric and instrumental leakage contributions given in Table 3 (worst case scenario), the contribution of the dust disk itself[5] and the different sources of background emission (sky and instrument).

We assume an overall instrumental throughput (including VLTI, GENIE and detectors) of 1% both in the L' and N bands. Table 4 gives the time required to detect a 20-zodi disk around a G2V star at 20 pc with a signal-to-noise ratio

---

[5] The part of the exozodiacal emission transmitted by the interference fringe pattern shown in Fig. 1 typically ranges between 30% and 40%.

Table 4. In the first part of the table, we compare the star and ex-ozodiacal disk fluxes to the thermal background, computed from its individual contributors (Paranal night sky, VLTI optical train and GENIE instrument) by integration over the field-of-view defined by a single-mode fiber ($\Omega = \lambda^2/S$). The target is a Sun-like star at 20 pc surrounded by a 20-zodi disk. The values are given in Jy at the central wavelength of the infrared atmospheric windows and "at the entrance of the Earth's atmosphere" (an equivalent emission is given for the background contributors as if they originated from outside the Earth atmosphere). Second part: signals in electrons per second actually detected at the GENIE science detector. The total shot noise is deduced, and used to compute the time needed for a photometric signal-to-noise ratio of 5.

	L'	N
Total stellar signal [Jy]	3.1	0.51
Total disk signal [Jy]	3.0×10^{-4}	5.1×10^{-4}
Sky brightness [Jy/as^2]	5.0	690
VLTI brightness [Jy/as^2]	115	21 300
GENIE brightness [Jy/as^2]	29	5320
Total bckg signal [Jy]	1.8	2550
Final stellar leakage [el/s]	1.0×10^4	1.5×10^3
Final disk signal [el/s]	3.6×10^2	4.1×10^3
Final bckg signal [el/s]	4.8×10^6	2.7×10^{10}
Shot Noise [el/s$^{1/2}$]	2.2×10^3	1.7×10^5
Time for SNR = 5 [s]	950	40 000

of 5. While the integration time in the L' band is reasonable (15 min), it is very large in the N band (11 h). In fact, the difficulty in the N band comes not only from the required integration time, but also from the huge contrast between the ex-ozodiacal and background fluxes (almost 10^7) at the output of the nuller. These two background-related issues are the main reasons for the choice of the L' band in the context of GENIE (Gondoin et al. 2004). Note that, even in the L' band, the required background calibration accuracy is challenging: in order to reach a final signal-to-noise ratio larger than 5, the background must be removed with an accuracy of 10^{-5}, which is within reach using the advanced background subtraction methods discussed in Sect. 5.1.

6.2. Final signal-to-noise ratio

In this section, we evaluate the global sensitivity of the GENIE instrument by simulating a 30-min observation of a Sun-like star at 20 pc surrounded by a 20-zodi disk. In Table 5, we first give the raw sensitivity of the nuller, i.e., without calibration of instrumental leakage (very conservative approach assuming that no convenient calibrator star can be found). In this case, the mean instrumental leakage fully contributes as a bias which adds to the exozodiacal disk signal that we want to detect. This implies that the mean instrumental leakage should be at least five times smaller than the disk contribution to ensure a safe detection. Table 5 shows that, depending on the model for atmospheric turbulence, the raw sensitivity ranges between 530 and 1800 zodis for a signal-to-noise ratio of 5 across the whole L' band. Instrumental leakage is the main contributor to the noise budget in that case. Note that shot

Fig. 10. Sensitivity of GENIE to dust disks around nearby main-sequence stars, expressed in units relative to the Solar zodiacal cloud. The simulations have been obtained with optimized AT-AT baselines in 2 h of integration. The availability of very small baselines (down to 8 m) allows us to reduce the contribution of geometric leakage and thus improves the detection levels of Fig. 9 at short distances.

circumstellar features such as exozodiacal disks. Ground-based nulling interferometry requires high-performance closed-loop control of atmospheric turbulence in the L' band, and extremely precise background subtraction in the N band. In this paper, we have computed the expected performance of state-of-the-art servo loops for piston, dispersion and intensity control, allowing the stabilization of the instrumental nulling ratio. Calibration procedures have been discussed to further remove stellar light from the nulled output of the instrument. This comprehensive study shows that an L'-band nuller such as GENIE at VLTI could detect exozodiacal disks about 50 to 100 times as dense as the Solar zodiacal cloud. This instrument will thus significantly improve the detection performance of current infrared and sub-millimetric facilities, and above all will peer into the currently inaccessible warm region of dust disks located within a few AU of nearby late-type dwarfs (typical Darwin/TPF-I targets).

The simulated performance of the nulling instrument critically depends on a number of noise contributions which could be improved in different ways. Geometrical leakage could be reduced by using short baselines, typically ranging between 8 and 40 m, while its calibration would be improved by obtaining accurate stellar diameter measurements at long baselines (>300 m) and/or precise photometry to derive diameters from surface-brightness relationships, and by extending the limb-darkening models towards the mid-IR wavelengths used by the nulling instruments. Instrumental leakage depends strongly on the ability to correct the effects of atmospheric turbulence, and would therefore benefit from advances in real-time control algorithms and compensation devices. Polarization errors, which have been discussed only briefly in this paper, could also be critical and need to be carefully addressed at the design level. Finally, advanced background subtraction methods such as the phase modulations techniques foreseen for the Darwin/TPF-I missions might further improve the overall performance of a ground-based nuller.

References

Absil, O. 2001, Diploma thesis, University of Liège, http://vela.astro.ulg.ac.be/themes/telins/harigs/

Absil, O., den Hartog, R., Erd, C., et al. 2003a, in Toward Other Earths: Darwin/TPF and the Search for Extrasolar Terrestrial Planets (ESA's Publication Division), SP-539, 317

Absil, O., Kaltenegger, L., Eiroa, C., et al. 2003b, in Toward Other Earths: Darwin/TPF and the Search for Extrasolar Terrestrial Planets (ESA's Publication Division), SP-539, 323

Absil, O., Karlsson, A., & Kaltenegger, L. 2003c, in Interferometry in Space, ed. M. Shao, Proc. SPIE, 4852, 431

Absil, O., Bakker, E., Schöller, M., & Gondoin, P. 2004, in New Frontiers in Stellar Interferometry, ed. W. Traub, Proc. SPIE, 5491, 1320

Allen, D., & Barton, J. 1981, PASP, 93, 381

Angel, J. 1989, in The Next Generation Space Telescope, ed. P. Bély, C. Burrows, & G. Illingworth (HST Sc. I., Baltimore), 81

Angel, J., & Woolf, N. 1997, ApJ, 475, 373

Arsenault, R., Alonso, J., Bonnet, H., et al. 2003, in Adaptive Optical System Technologies, ed. P. Wizinowich, & D. Bonaccini, Proc. SPIE, 4839, 174

Beichman, C., Bryden, G., Rieke, G., et al. 2005, ApJ, 622, 1160

Beichman, C., Woolf, N., & Lindensmith, C. 1999, TPF: A NASA Origins Program to Search for Habitable Planets (Pasadena, CA: Jet Propulsion Laboratory), JPL 99-3

Bracewell, R. 1978, Nature, 274, 780

Chazelas, B., Brachet, F., Bordé, P., et al. 2005, Appl. Opt., accepted

Claret, A. 2000, A&A, 363, 1081

Claret, A., Díaz Cordovés, J., & Giménez, A. 1995, A&AS, 114, 247

Colavita, M., Wizinovich, P., & Akeson, R. 2004, in New Frontiers in Stellar Interferometry, ed. W. Traub, Proc. SPIE, 5491, 454

Conan, J.-M., Rousset, G., & Madec, P.-Y. 1995, J. Opt. Soc. Am. A, 12, 1559

Dermott, S., Grogan, K., Holmes, E., & Wyatt, M. 1998, in Proc. of the Exo-zodiacal Dust Workshop, ed. D. Backman, L. Caroff, S. Sanford, & D. Wooden (NASA/CP), 10155, 59

Fors, O., Richichi, A., Núñez, J., & Prades, A. 2004, A&A, 419, 285

Fridlund, M. 2000, ESA bulletin, 103, 20

Glindemann, A., Albertsen, M., Andolfato, L., et al. 2004, in New Frontiers in Stellar Interferometry, ed. W. Traub, Proc. SPIE, 5491, 447

Gondoin, P., Absil, O., den Hartog, R., et al. 2004, in New Frontiers in Stellar Interferometry, ed. W. Traub, Proc. SPIE, 5491, 775

Herbst, T., & Hinz, P. 2004, in New Frontiers in Stellar Interferometry, ed. W. Traub, Proc. SPIE, 5491, 383

Karlsson, A., & Mennesson, B. 2000, in Interferometry in Optical Astronomy, ed. P. Léna, & A. Quirrenbach, Proc. SPIE, 4006, 871

Kelsall, T., Weiland, J., Franz, B., et al. 1998, ApJ, 508, 44

Kervella, P., Thévenin, F., Ségransan, D., et al. 2003, A&A, 404, 1087

Kervella, P., Thévenin, F., di Folco, E., & Ségransan, D. 2004, A&A, 426, 297

Kolmogorov, A. 1941, Doklady Akad. Nauk. S.S.S.R., 30, 229

Koresko, C., Mennesson, B., Serbyn, E., et al. 2003, in Interferometry for Optical Astronomy II, ed. W. Traub, Proc. SPIE, 4838, 625

Kuchner, M., & Brown, M. 2000, PASP, 112, 827

Kuchner, M., Brown, M., & Koresko, C. 1998, PASP, 110, 1336

Lawson, P., & Dooley, J. 2005, Technology Plan for the Terrestrial Planet Finder Interferometer (Pasadena, CA: Jet Propulsion Laboratory), JPL 05-5

Lay, O. 1997, A&AS, 122, 535

Lay, O. 2004, Appl. Opt., 43, 6100

Léger, A., Mariotti, J., Mennesson, B., et al. 1996, Icarus, 123, 149

Mathar, R. 2004, Appl. Opt., 43, 928

Meisner, J., & Le Poole, R. 2003, in Interferometry in Optical Astronomy II, ed. W. Traub, Proc. SPIE, 4838, 609

Mennesson, B., Ollivier, M., & Ruilier, C. 2002, J. Opt. Soc. Am. A, 19, 596

Mérand, A., Bordé, P., & Coudé du Foresto, V. 2005, A&A, 433, 1155

Ollivier, M. 1999, Ph.D. Thesis, Université de Paris XI

Quirrenbach, A. 1999, in Principles of Long Baseline Stellar Interferometry, ed. P. Lawson (JPL publ.), 71

Roddier, F. 1981, in Progress in optics, ed. E. Wolf, Vol. XIX, North-Holland, Amsterdam, 281

Ruilier, C., & Cassaing, F. 2001, J. Opt. Soc. Am. A., 18, 143

Serabyn, E., Booth, A., Colavita, M., et al. 2004, in New Frontiers in Stellar Interferometry, ed. W. Traub, Proc. SPIE, 5491, 806

Serabyn, E., & Colavita, M. 2001, Applied Optics, 40, 1668

Stankov, A., Kaltenegger, L., & Eiroa, C. 2005, ESA/ESTEC internal publication DMS/SCI-A/DARWIN/289

ten Brummelaar, T. 1995, Opt. Commun., 115, 417

Vérinaud, C., & Cassaing, F. 2001, A&A, 365, 314

Wilhelm, R., & Gitton, P. 2003, in Toward Other Earths: Darwin/TPF and the Search for Extrasolar Terrestrial Planets (ESA's Publication Division), SP-539, 659

Young, A., Milone, E., & Stagg, C. 1994, A&AS, 105, 259